Advances in Geo-Energy Research

Vol. 20, No. 1, p. 71-84, 2026

Original article

The combined effects of pressure decline and gas withdrawal in underground hydrogen storage: A pore-scale experimental study

Waleed Dokhon*, Branko Bijeljic, Martin J. Blunt

Department of Earth Science and Engineering, Imperial College, London SW7 2BP, United Kingdom

Keywords:
Critical gas saturation
pressure decline
gas expansion
pore-scale
gas storage

Cited as:
Dokhon, W., Bijeljic, B., Blunt, M. J. The combined effects of pressure decline and gas withdrawal in underground hydrogen storage: A pore-scale experimental study. Advances in Geo-Energy Research, 2026, 20(1): 71-84.
https://doi.org/10.46690/ager.2026.04.06

Abstract:
Hydrogen withdrawal from subsurface porous formations is expected to experience fast pressure decline rates, yet the pore-scale effects remain poorly explored. This study examines how pressure decline and simultaneous brine influx affect the withdrawal of stored hydrogen in a water-wet Bentheimer sandstone, representing hydrogen storage in saline aquifers. Brine was injected while the outlet pressure was reduced at a fixed rate. Two initial conditions were tested: A high gas saturation, representative of regions above the gas-water contact, and a residual gas saturation, representative of regions below it. Micro-computed tomography was used to quantify gas distribution, connectivity, and the dominant displacement mechanism during pressure decline with continued brine influx. The observations show that capillary pressure can increase during pressure decline, showing that the main displacement mechanism is drainage, even as brine is flowing. The gas saturation increased through the expansion of trapped gases, and large gas clusters connected to the outlet and were produced by expansion. No imbibition displacement was seen despite the high gas saturation reached by expansion. When pressure decline began from residual conditions, the gas saturation increase was proportional to the magnitude of pressure decline, whereas starting from a high gas saturation led to larger residual clusters and greater connectivity. These observations suggest that under continuous pressure decline, local capillary pressure can increase, preventing imbibition displacement of gas by water. This makes the interpretation of laboratory experiments to find the critical gas saturation challenging, as it depends on the displacement process. Gas production occurs primarily through expansion-driven drainage rather than through normal displacement.

1. Introduction

Subsurface natural gas storage in geological formations has long been used to ensure a continuous source of energy. In the energy transition, underground hydrogen storage (UHS) is important to store large volumes of hydrogen produced from excess renewable energy (Heinemann et al., 2021; Zivar et al., 2021; Miocic et al., 2023; Mwakipunda et al., 2025).

Given the expected demand for rapid power delivery, UHS in porous formations may experience fast withdrawal over short periods due to the intermittent nature of renewable energy. This makes multiphase flow under pressure decline and gas expansion an important area of study (Dokhon et al., 2024). During hydrogen withdrawal from storage, trapped gases can remobilise if the gas saturation increases to a level at which a connected gas path, known as the critical gas saturation (S_{gc}), is reached. This was first studied for oil and gas reservoirs in an improved hydrocarbon recovery strategy known as post-waterflooding depressurisation that

Yandy Scientific Press

*Corresponding author.
E-mail address: waleed.dokhon21@imperial.ac.uk (W. Dokhon); b.bijeljic@imperial.ac.uk (B. Bijeljic); m.blunt@imperial.ac.uk (M. J. Blunt).

Received January 19, 2026; revised February 22, 2026; accepted March 10, 2026; available online March 15, 2026.

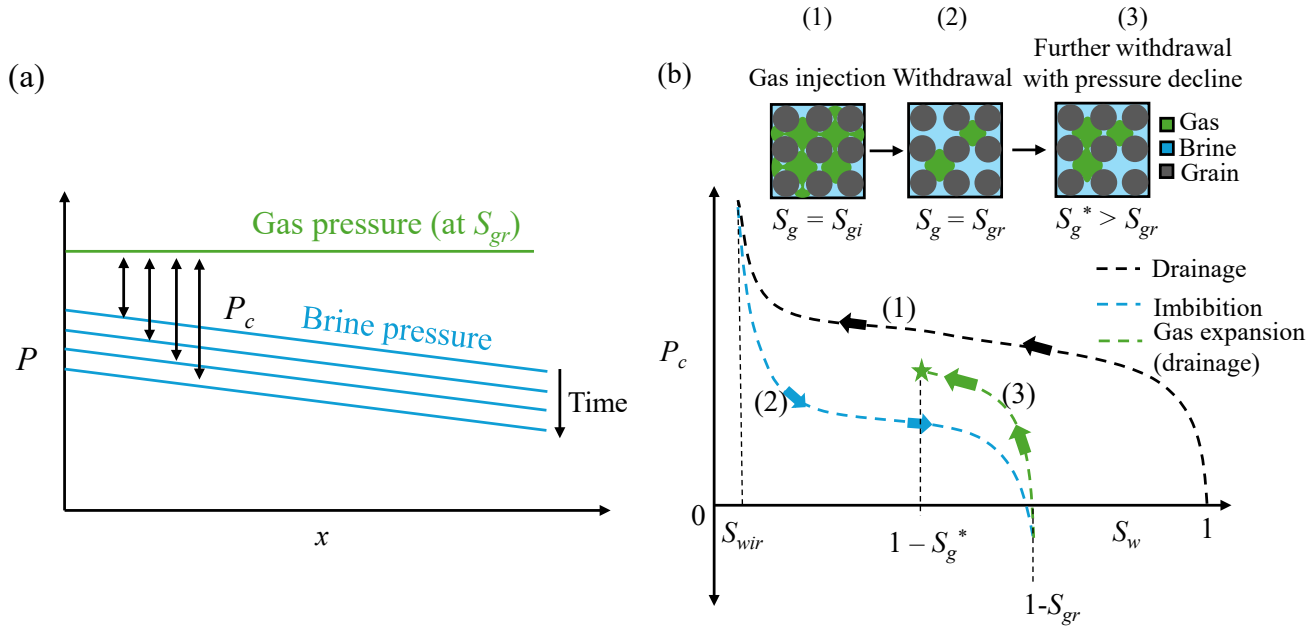

Fig. 1. (a) A schematic of phase pressures as a function of distance and (b) the corresponding conceptual $P_c(S_w)$ diagram after drainage (black) and imbibition (blue).

involves reducing the reservoir pressure below the bubble point by continuous withdrawal and without pressure maintenance (Drummond et al., 2001). The gas bubbles that exsolve under these conditions are initially trapped. Continued withdrawal and pressure decline cause the bubbles to expand until a connected path forms; that point defines S_{gc}.

Measuring S_{gc} has long been important, with many laboratory and modelling studies. Most of these studies have considered natural gas exsolution from oil. Table 1 summarises previous experimental studies of S_{gc}, outlining the methods used for its measurement. The experimental procedure typically involves a liquid phase (e.g., brine) saturated with gas, followed by an imposed pressure decline that drives gas exsolution and expansion. Laboratory methods to determine S_{gc} vary. In oil-gas depletion tests, one method identifies S_{gc} when the flowing gas-oil ratio (GOR) increases from the dissolved-gas GOR from material balance (Kamath and Boyer, 1995). Another method uses X-ray CT imaging to assess gas connectivity, either by the onset of continuous gas production and a sharp increase in gas saturation (Egermann and Vizika, 2000), or a topological percolation criterion (Euler characteristic crosses zero) (Berg et al., 2020).

When pressure decline starts from a residual gas saturation, as may be seen in carbon dioxide storage and UHS, the S_{gc} is considerably larger than seen in a solution gas drive where the initial condition is no gas present. For instance, Moghadasi et al. (2025) used X-ray micro-CT imaging to determine a S_{gc} of approximately 0.61 for carbon dioxide during pressure decline. This suggests that S_{gc} is a function of the initial conditions and the displacement process.

Depending on the field strategy, the onset of depressurisation and the initial condition (S_{gi} or S_{gr}) can show different flow or trapping behaviours (Egermann and Vizika, 2000). In post-waterflooding depressurisation, pressure decline is used after oil has reached its residual saturation S_{or} so that gas exsolved by solution-gas drive contributes most to production (Naylor et al., 2000). For CO_2 storage, pressure decline may occur during a leak or CO_2 migration (Moghadasi et al., 2025); above the gas-water contact (GWC), the initial state is $S_g = S_{gi}$ (high gas saturation), while below the GWC/free-water level (FWL), the gas is at residual saturation. Both zones will decline in pressure depending on the continuous phase. Above the GWC, a connected gas phase may stay mobile and continue expanding; below it, disconnected ganglia must expand and percolate to reach S_{gc}. Testing the effect of pressure decline at two initial conditions (S_{gi} and S_{gr}) is therefore appropriate for such systems. The same logic applies to UHS.

While several studies have investigated gas expansion and S_{gc}, no work has examined how this process behaves at the pore-scale under continuous pressure decline with brine influx under capillary-dominated conditions relevant to UHS in saline aquifers. In other systems, CO_2 and methane solubility in the aqueous or oil phase is much higher (Bagchi et al., 2025), whereas H_2 in brine has very low solubility (Chabab et al., 2020), making gas exsolution a weak contributor to the behaviour. Therefore, gas expansion and displacement in the H_2-brine system may be distinct. Fig. 1 shows the pore-scale sequences expected in a water-wet homogeneous porous medium with pressure decline and continuous brine influx. After drainage and imbibition, the gas is at S_{gr} and remains as disconnected ganglia. With pressure decline, brine pressure decreases, while the gas pressure remains relatively unchanged, as it is disconnected. As a result, the local capillary pressure increases ($P_c = P_g - P_w$), which is a drainage displacement. This drainage process is different from external drainage by injection (Kamath and Boyer, 1995) and since the residual gas saturation can be high, this may resemble a normal percolation

Table 1. A summary of previous experimental studies for the measurement of the critical gas saturation.

Reference	Method	Pressure decline rate (kPa/min)	Rock & fluids system	Measurement of S_{gc}	S_{gc}
Kamath and Boyer (1995)	Tested depletion on rock samples at high and low pressure decline rates; used CT to check saturation uniformity; measured supersaturation and S_{gc}	0.479 (Low) 0.096 (High)	Colton sandstone; methane + model oil (no brine)	S_{gc} taken where flowing GOR first deviates from the dissolved GOR during pressure decline (plots of GOR vs S_g)	0.1 at both pressure decline rates
Egermann and Vizika (2000)	Dynamic depressurisation by outlet pressure decline; *in situ* S_g profile by CT; tested different drawdown rates. Two initial conditions were tested: Fully oil saturated and at S_{wi}	16.7	Palatinate sandstone; brine + C1/C7 model oil	From the jump on the stabilised S_g profile (mobility threshold) and CT evidence of bubble connection vs dispersed-bubble mobilisation	0.17-0.24 (at S_{wi}) 0.48-0.50 (at $S_w = 0$)
Petersen Jr et al. (2004)	Depletion was tested at three rates (low, moderate, and high); CT monitoring of S_g and production	0.55 (Low) 1.43 (Moderate) 3.50 (High)	Brent sandstones; live oils; tested at S_{wi} and at S_{or}	Pressure decline first, followed by water flooding. The onset of continuous gas production from the core (supported by CT profiles)	0.05-0.134 (depending on depletion rates and initial oil saturation)
Zuo et al. (2012)	CO_2 exsolution during depressurisation; CT-monitored; used both high and low pressure decline rates	20 (Low) 1,000 (High)	Berea & Mount Simon sandstones; CO_2-saturated brine	Onset of large pressure drop fluctuations across the core (turning point in ΔP vs S_g curve)	0.11-0.155. (Higher pressure decline rates resulted in higher S_{gc})
Sun et al. (2018)	Sandpack depletion (heavy/foamy oil tests); three constant pressure decline rates	6.7 (Low) 13.3 (Moderate) 26.7 (High)	Long sandpack (50 cm); live heavy oil (Venezuelan) saturated with CH_4/CO_2; foamy oil behaviour	S_{gc} at the pressure where cumulative GOR begins to increase linearly (onset of continuous gas phase)	0.0363 (at low rate) 0.0588 (at high rate)
Berg et al. (2020)	Micro-CT determination of percolation threshold during pressurization vs depletion scenarios; direct 3D imaging and topology analysis	Stepwise pressure decline (depressurise then re-pressurise or further deplete)	Bentheimer sandstone; live oil model	Euler characteristic zero-crossing of the gas phase (percolation threshold) taken as S_{gc}	0.2 (in depletion case)
Al-Masri and Shapiro (2021)	CT-based method to measure S_{gc} and oil flow under pressure decline in chalk; stepwise pressure reductions with connected viscometer	Stepwise pressure decline	Stevns Klint outcrop chalk; Dan & Valdemar reservoir chalks; C1-C7/C10 oils (no brine)	Critical point confirmed by the appearance of pressure drop fluctuations across the viscometer during displacement; steady state re-established at S_{gc} (also measured by CT)	0.08-0.26 (depending on chalk and mixture (e.g., 9%-26% Upper Cretaceous; 8%-10% Lower Cretaceous))
Moghadasi et al. (2025)	Micro-CT imaging of Bentheimer sandstone during stepwise pressure depletion (10>8>6>5 MPa); paired with pore-network modelling for different rock properties to track the gas clusters and predict remobilisation	Stepwise pressure decline	Bentheimer sandstone; CO_2-brine, water-wet; 50 °C	S_{gc} taken from the first connected gas cluster from CT images; Euler number trend. S_{gc} from the model is when a gas cluster spans inlet to outlet	0.61 ± 0.02 (inferred between 6-5 MPa during pressure decline)

Notes: GOR is the gas-oil ratio, S_g is the gas saturation; S_{wir} is the irreducible water saturation; S_{wi} is the initial water saturation; S_{or} is the residual oil saturation; and ΔP is the pressure drop.

process in which each ganglion independently invades areas with the lowest entry pressure.

As drainage by gas expansion continues and ganglia connect to the outlet, gas production starts. However, this gas production is not due to displacement of gas by water, imbibition, but rather to gas expansion towards the drawdown source (Alobaidan et al., 2025). Gas connected to the outlet therefore reduces in pressure and continues expanding as long as the system pressure declines. For this reason, the concept and measurement of S_{gc} can be reconsidered: Under continuous pressure decline, the flow remains drainage-controlled, and gas production occurs through expansion-driven drainage rather than imbibition. This is why no prior study has shown a reduction in S_g by imbibition after reaching S_{gc} during pressure decline. S_{gc} is best interpreted as an inlet-to-outlet connectivity threshold. Once such connectivity is established, gas pressure can decline with the outlet pressure, which may reduce P_c and drive imbibition displacement. However, the subsequent regime (i.e., after imbibition) depends on the changes of P_g and P_w under drawdown. Therefore, the measured S_{gc} is path dependent.

In this work, pore-scale hydrogen-brine displacement experiments in water-wet Bentheimer sandstone are performed to investigate the combined effects of pressure decline and brine injection. Brine is injected at a constant flow rate while a programmed outlet pressure decline rate of 1 kPa/min is applied. At the field-scale this would represent, for instance, a 3 MPa pressure drop at the well over a period of just over two days, representing a rapid depressurisation; however, note that in UHS representative pressure declines during production are orders of magnitude faster than seen during solution gas drives in oil reservoirs, where production continues over years to decades. This rapid depressurisation can result in an alternation of displacement regimes between drainage and imbibition depending on which phase is continuous and which is trapped. In water-wet systems the brine is typically continuous so P_w declines with drawdown. If gas is connected (e.g., above the GWC) P_g also declines and the displacement may be imbibition, whereas disconnected gas below the GWC is trapped at its own pressure while P_w decreases, increasing P_c and promoting drainage displacement. In field-scale simulation, the flow properties used need to represent the local displacement process. Near the wellbore, extreme pressure gradients are likely, while the distribution of flow rates and pressure decline will depend on local heterogeneity and wettability. This work shows that the local displacement is principally expansion-driven drainage. The next section will delineate the conditions under which this is likely to occur.

Two initial states are tested: High gas saturation ($S_g = S_{gi}$), representative of regions above the GWC, and residual gas saturation ($S_g = S_{gr}$), representative of regions below the GWC/FWL. Two brine flow rates are tested (0.01 and 0.05 mL/min) to vary the capillary number. X-ray micro-CT is used to image the sample at different pressure drops. The saturation profiles, ganglia count, volume distributions, and gas connectivity are analysed. The start of gas production is defined by calculating the fractional pressure drop and comparing it with the gas expansion factor from the images.

2. Theory

This study will consider expansion in the absence of advective displacement and dissolution. The assumptions are:

1) Isothermal conditions and spatially uniform pore pressure;
2) The number of hydrogen moles is constant during expansion;
3) Rock and brine compressibilities are negligible so that the pore volume, V_p, is constant;
4) Hydrogen behaves nearly ideally so that the Z (compressibility factor) factor is constant over the pressure interval considered.

The material balance for the gas phase is (Ahmed, 2018):

$$n = \frac{PV_g}{ZRT} = \frac{PS_gV_p}{ZRT} \tag{1}$$

where n is the number of moles; P is the pore pressure, Pa; V_g is the gas volume, m^3; R is the gas constant, J/(mol·K); T is the absolute temperature, K; S_g is the gas saturation; and V_p is the pore volume, m^3. With n, V_p, Z, and T constant, the product PS_g remains constant during expansion:

$$PS_g \approx P(t)S_g(t) \approx \text{constant} \tag{2}$$

where t is time. If the pore pressure declines approximately linearly at a rate > 0, then the pressure at any time during pressure decline, $P(t)$, is:

$$P(t) = P_0 - \dot{P}t \tag{3}$$

where P_0 is the initial pressure, Pa. Combining Eqs. (2) and (3) provides a simple prediction for the evolution of gas saturation with time:

$$S_g(t) = S_{g0}\frac{P_0}{P_0 - \dot{P}t},\ 0 < t < \frac{P_0}{\dot{P}} \tag{4}$$

where S_{g0} is the gas saturation at P_0. In intermediate stages where disconnected smaller ganglia coexist with larger clusters, the pore pressure in Eq. (4) should be interpreted as the pressure of the continuous phase. In water-wet rocks, the brine is typically continuous, so P_w declines with drawdown and Eq. (4) describes the expansion-driven evolution of the trapped (disconnected) gas saturation as long as the trapped gas pressure remains approximately constant relative to the declining brine pressure. Deviations from the linear trend predicted by Eq. (4) are expected if the controlling pressure field switches (e.g., brine becomes locally disconnected) or if a large outlet-connected gas cluster dominates the drawdown source. In the latter case, the local P_c of trapped gas will remain unchanged, and the trapped gas expansion predicted by Eq. (4) would be overestimated.

If S_{g0} is taken as the residual gas saturation S_{gr}, and the target gas saturation as S_{gc}, then the time required to reach S_{gc} is:

$$t = \frac{P_0}{\dot{P}}\left(1 - \frac{S_{gr}}{S_{gc}}\right) \tag{5}$$

Eq. (5) is valid provided the assumptions discussed above hold and before other physical effects (e.g., capillary redistri-

bution, dissolution, or measurable rock/brine compressibility) become important.

In previous work (Dokhon et al., 2024), the expansion number was defined as the ratio of a pressure change due to expansion to Darcy flow over a characteristic (or reference) length L:

$$\begin{aligned} \Delta P_D &= \frac{qL\mu}{K} \\ \Delta P_E(t) &= \dot{P}t \\ E(t) &= \frac{\Delta P_e}{\Delta P_D} = \frac{K\dot{P}t}{qL\mu} \end{aligned} \tag{6}$$

where ΔP_D is the pressure change due to displacement, Pa; ΔP_E is the pressure change due to expansion, Pa; K is the absolute permeability, m^2; $E(t)$ is the expansion number at time t, q is the Darcy velocity of the brine, m/s; and μ is the brine viscosity, Pa·s. Previously, time t was equated to be the time needed for displacement (Dokhon et al., 2024) by substituting t with the time required to displace one pore volume over the reference length L, $L\phi/q$:

$$E = \frac{\Delta P_E}{\Delta P_D} = \frac{K\dot{P}\phi}{q^2\mu} \tag{7}$$

In this study, E was ~1,800 at 0.01 mL/min and ~70 at 0.05 mL/min (the pressure decline rate was 16.7 Pa/s).

Additionally, the expansion number E is evaluated at the time when S_{gr} reaches S_{gc} and using Eq. (5):

$$E(S_{gc}) = \frac{KP_0}{qL\mu}\left(1 - \frac{S_{gr}}{S_{gc}}\right) \tag{8}$$

Physically, this expression is an indication of how much expansion has to act before gas reaches the mobile gas saturation. If S_{gr}/S_{gc} is close to 1, there is little pore volume available for expansion, and $E(S_{gc})$ approaches zero (i.e., Darcy displacement will dominate once gas becomes mobile). Conversely, if S_{gr}/S_{gc} is small, expansion can act over a greater drop in pore pressure with no gas flow, because the trapped gas continues to expand within the pores and has not reached the mobility threshold.

The experimental case corresponds to the following parameters: Sample radius $r = 6.3 \times 10^{-3}$ m, length $L = 0.0361$ m, with permeability $K = 1$ D (9.87×10^{-13} m^2). The initial pore pressure where the gas is capillary trapped was $P_0 = 3.5$ MPa, the flow rate $Q = 0.01$ mL/min, with brine viscosity = 1.5×10^{-3} Pa·s, and hydrogen-water interfacial tension $\sigma = 0.075$ N/m. The residual and critical gas saturations for the current case were taken as $S_{gr} = 0.40$ and $S_{gc} = 0.65$, respectively. This leads to a value of $E = 2 \times 10^4$ which indicates that expansion dominates.

This analysis shows that, at the pore-scale, gas expansion is the dominant physical process. Even though brine is injected, the brine pressure gradient is smaller than the absolute pressure drop, indicating that expansion governs the pore-scale behaviour.

3. Experimental design and methodology

3.1 Rock samples and fluids

The experiments were performed on a cylindrical sample of Bentheimer sandstone (12.6 mm diameter, 36.1 mm length). Bentheimer was selected for its mineralogical simplicity, homogeneity, and reproducible petrophysical behaviour that makes it a benchmark for pore-scale imaging and flow; the narrow porosity and permeability ranges and low clay content aid image segmentation and interpretation (Andrew et al., 2014; Peksa et al., 2015, 2017; Al-Yaseri et al., 2023). The aqueous phase was 26 wt% potassium iodide (KI) brine to provide sufficient contrast in the micro-CT images. The gas phase was H_2 (99.999% purity). The brine was pre-equilibrated with H_2 in a stirred reactor vessel at 4 MPa and room temperature for ~ 3 days before the experiment.

3.2 Sample assembly and flow loop

The rock sample was mounted vertically in a Viton rubber sleeve. A water-wet ceramic porous plate (entry pressure ~ 100 kPa; 12.6 mm diameter) was fixed to the outlet face to (i) stop gas from leaving through the outlet during drainage displacement, and (ii) distribute the brine flux during imbibition. The sleeve was wrapped with aluminium tape to limit hydrogen diffusion into the confining fluid. PEEK tubes connected the inlet and outlet to programmable syringe pumps. A differential pressure transducer was connected near the inlet and outlet ports; both lines were filled with brine before use.

Four syringe pumps were used: A hydrogen pump (gas drainage from the top), a brine pump (H_2-saturated brine through the porous plate at a constant flow rate), a back-pressure pump (set outlet pressure and applied the programmed pressure decline rate), and a confining pump (kept the confining pressure at 6 MPa).

The reactor vessel used to saturate the brine was a ~ 1 L Hastelloy vessel with a dip tube. About 0.7 L of brine was loaded, the headspace was purged with H_2, then H_2 was compressed to 4 MPa. The brine pump was refilled from the dip tube to draw H_2-saturated brine from the bottom. Fig. 2 provides an overview of the apparatus and flow loop.

3.3 Displacement and pressure decline protocol

The goal is to see how an imposed pressure decline (PD) changes the outcome of gas displacement by brine. The two flow rates used were 0.01 and 0.05 mL/min.

(1) Initial preparation

The confining fluid was first pressurised to compress the sleeve to the sample. A dry scan was acquired and the apparatus was checked for leaks. Air was removed by injecting the prepared brine (top and bottom directions as needed) for ~ 200 PV to displace any residual air pockets. A wet scan confirmed full brine saturation. Brine permeability was then measured by injecting the brine solution at multiple flow rates and recorded the corresponding pressure drops; the brine permeability was measured as 900 mD (±100 mD).

(2) Drainage and brine displacements

Before each brine injection (imbibition), drainage was first performed to initialise the initial gas saturation (S_{gi}) targeting an S_{gi} above ~ 0.80 (Raeesi et al., 2014; Dokhon et al., 2025).

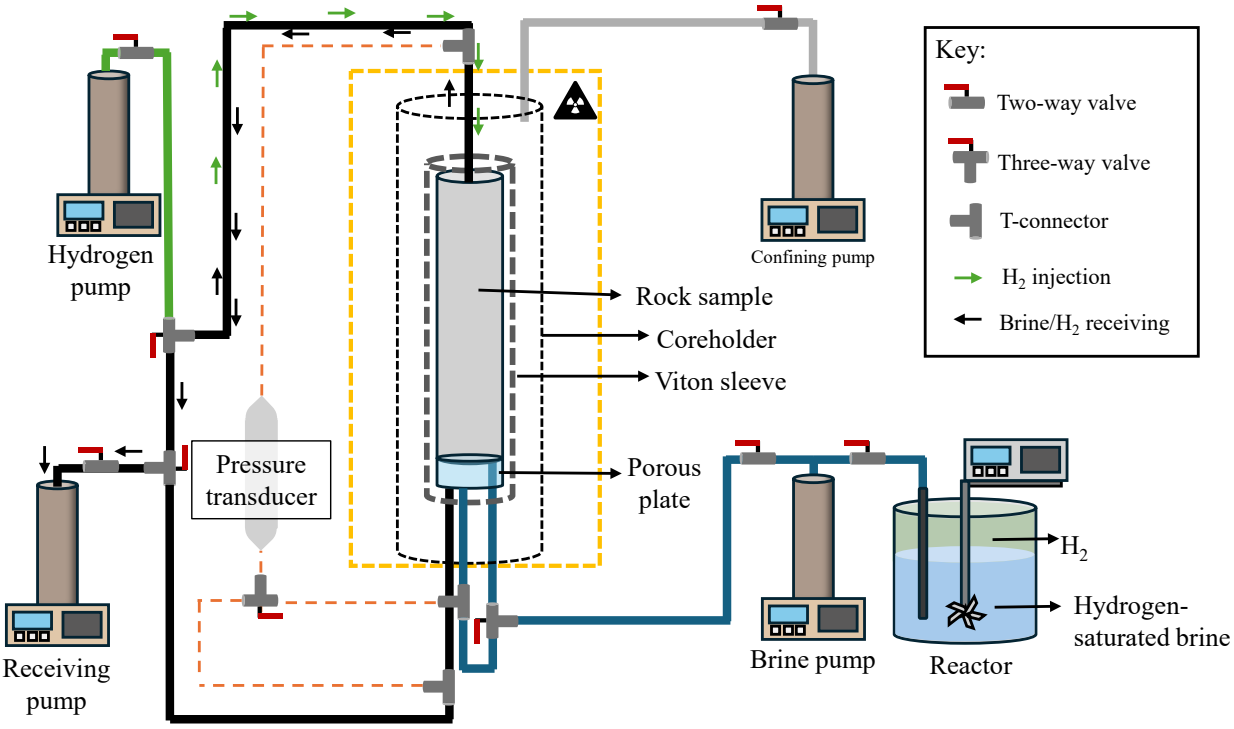

Fig. 2. Schematic of the experimental apparatus, showing the rock sample with a water-wet ceramic porous plate at its base. A pressure transducer was connected to the inlet and outlet points closest to the sample (orange dashed lines).

Brine injections were then conducted in two ways: Without pressure decline (baseline) and with pressure decline, where a constant outlet pressure decline rate of 1 kPa/min was applied by the back-pressure pump while the brine pump was kept at a constant flow rate. Pressure decline was started either at the beginning of brine injection or after residual gas saturation had been reached, to test the impact of when the pressure decline occurs (specifically pressure decline when the gas was initially connected vs when the gas was initially capillary trapped).

(3) Pressure decline

The pressure drops used in the tests covered a broad practical range, from $\Delta P \approx 200$ kPa up to $\approx$ 1,000 kPa, depending on the starting pressure and the injected pore volumes. The results are reported in terms of the fractional pressure drop (i.e., $\Delta P/P_0$) for clarity and comparison across stages. A map of the displacement process and stages is shown in Fig. 3. Cases 1 and 3 start brine injection to displace the initial gas saturation, then continue displacement but with pressure decline (PD at S_{gr}). Cases 2 and 4 start brine injection with pressure decline from the start (at S_{gi}).

3.4 X-ray micro-CT imaging

A helical micro CT scanner (Heliscan) was used to image the whole sample at 9.6 μm/voxel to build saturation profiles and ganglia size statistics across the length of the sample and for pore-scale analysis (interfaces and topology/connectivity). Images were taken at the main stages of each sequence (before displacement baselines, after each pressure decline step, and after the brine injection steps).

3.5 Image pre-processing and segmentation

Reconstructed images were corrected for beam hardening, cropped to the rock, and normalised to a consistent greyscale for each resolution by converting the images to 8-bit (Higgs et al., 2024). A non-local means filter was used to reduce noise (Baldwin et al., 1996), then all wet scans were registered to the dry scan to build a pore mask. For the overall gas saturation profile from the whole-sample images, the gas and brine were segmented by intensity, while the rock phase was taken from the registered dry image. For pore-scale analysis (interfaces, topology), marker-controlled watershed was used to better capture the phase contacts (Brown et al., 2014). The porosity was measured from segmenting the dry image ($\phi \approx 0.19$), giving a pore volume $V_p \approx 8.5 \times 10^{-7}$ m^3 (0.85 cm^3).

3.6 Accounting for dissolution and exsolution of hydrogen

Because the brine was pre-equilibrated with H_2 at 4 MPa, hydrogen dissolution during displacement was reduced, but was not zero. The applied pressure decline extends the displacement time, and two effects matter. First, trapped gas bubbles can be at a pressure higher than the local pore pressure, so some dissolution into the brine is expected, especially when 2 or more pore volumes of brine are injected (Gao et al., 2023). Second, the brine pump slightly pressurises the brine above the pore pressure for injection, which raises the maximum possible dissolved gas concentration and drives additional dissolution at the inlet (Dokhon et al., 2025). However, as the brine

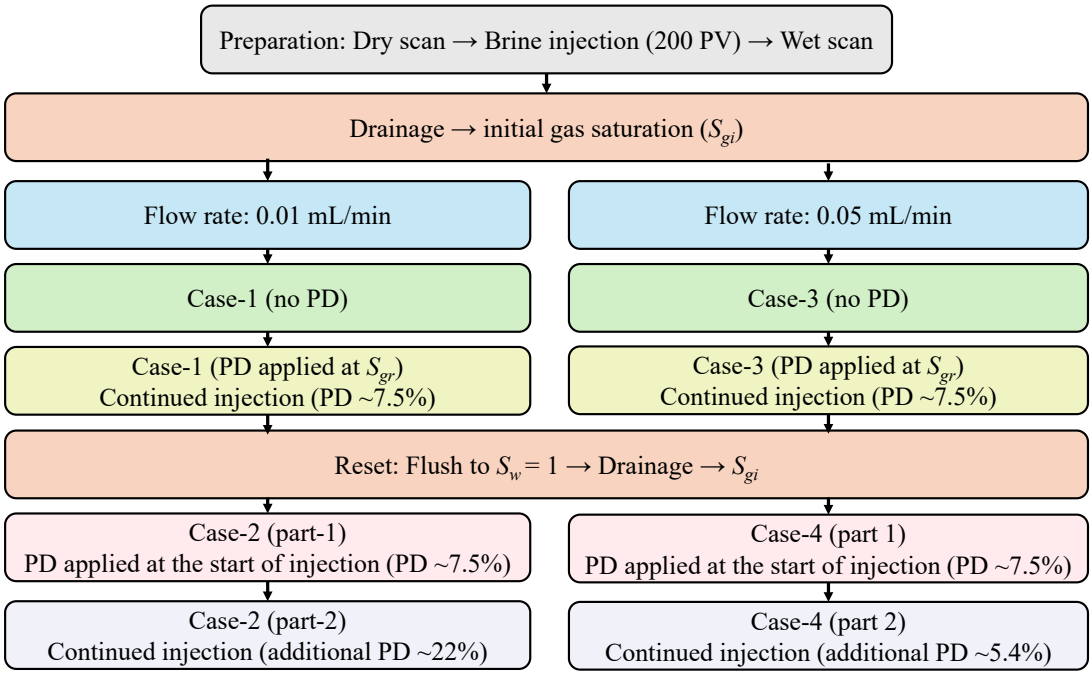

Fig. 3. The overall sequence of displacement with and without pressure decline and at two flow rates (left panel is for the 0.01 mL/min flow rate and the right panel is for the 0.05 mL/min flow rate).

moves through the sample, it re-equilibrates with the gas in the sample, and the dissolution effect reduces along the length of the sample (Jangda et al., 2023). In practice, this means the inlet side may show transient dissolution, while the outlet side tends to be closer to a steady saturation. Therefore, the saturation profile was checked and the uniform section of the sample was used as the representative S_g for calculations. Additionally, the amount of gas that would be dissolved if the brine had not been pre-equilibrated was calculated and compared with the observed dissolution when pre-equilibrated brine was used.

The expected gas exsolution was quantified from a pressure drop using Henry's law with a linear slope from the 4 MPa solubility (0.00918 mol/kg at 23 °C in this work (Zhu et al., 2022)). When the pressure drops from P_0 to P_i, the difference in equilibrium solubility corresponds to the amount of gas moles exsolved, $\Delta n_{exsolved}$:

$$\Delta n_{exsolved} = k m_w (P_0 - P_i) \tag{9}$$

where k is the solubility constant, mol/kg; m_w is the mass of brine, kg; P_i is the current pressure and P_0 is the initial pressure, Pa. The moles of hydrogen are converted to gas volume at P_i with the ideal-gas relation at 298.15 K. The brine mass is estimated from the baseline water saturation and the known pore volume. The exsolved gas contribution to the saturation, $\Delta S_{g,\ exsolved}$, is:

$$\Delta S_{g,\ exsolved} = \frac{V_{exsolved}}{V_P} \tag{10}$$

where $V_{exsolved}$ is the volume of hydrogen that comes out of brine at the lower pressure. The exsolved volume of hydrogen was compared with the measured change in S_g from images (before and after pressure decline) to compare contributions of exsolved gas and expanded gas.

3.7 Measurements from micro-CT images

Gas saturation was measured by masking the rock phase from the dry image and applying that mask to the corresponding image during displacement. This avoids ambiguity from segmenting the brine phase, whose greyscale can partly overlap with the rock. Saturation profiles were reported slice wise and for the whole sample.

To study the volume distribution and the change in the number of gas clusters across the whole sample, each ganglion was labelled. This allowed the observation of the reduction or growth of the gas ganglia population and how the distribution shifts with pressure decline. The connectivity of the gas phase was quantified with a simple topological measure (Euler characteristic) for the whole sample. The interfacial areas were measured from a 1,000 × 1,000 × 1,000 voxel sub-volume.

3.8 Operating conditions, quality control and uncertainty

Unless stated otherwise, the pore pressure was 4 MPa. The confining pressure was 6 MPa and the temperature was 23 °C. The flow rates were 0.01 and 0.05 mL/min. Using a brine viscosity of 1.5×10^{-3} Pa·s and a H_2-brine interfacial tension of 0.075 N/m, the capillary number during injection is on the order of $\sim 10^{-8}$-10^{-7} (capillary-dominated regime (Krevor et al., 2015)). The accuracy of the recorded pump pressures was ±1.5 kPa, and the differential pressure transducer had ±0.3 kPa resolution. A high resolution scan (3.1 μm/voxel) was used to check the porosity difference with the 9.6 μm/voxel

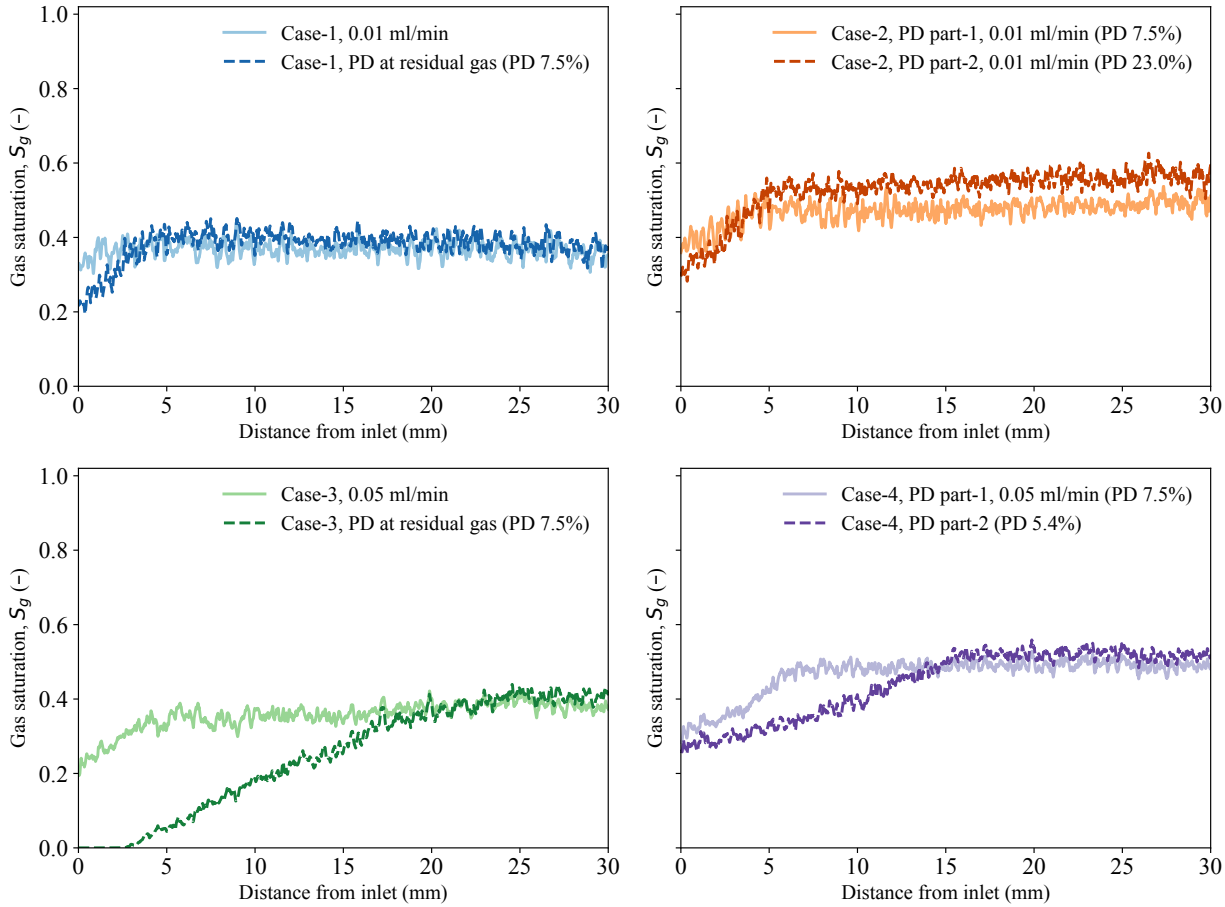

Fig. 4. Gas saturation profiles along the sample length for all displacement cases. Brine was injected from left to right. The fractional pressure drop is indicated in the legends.

scan and showed a $\sim \pm 2$ % difference, which was accounted for in the saturation uncertainty. Gas dissolution was assessed by checking the raw images to see if the brine inlet side had capillary trapped ganglia completely displaced. In gas expansion, if a gas ganglion is connected to the outlet (production) side, it can expand and get produced. This is especially true if pressure decline was imposed when the gas was initially connected (S_{gi}).

4. Results and discussion

4.1 Effect of pressure decline during displacement on gas volume

To compare the effect of pressure decline on gas saturation, the gas saturation profiles were examined along the full sample length for all the displacement cases. Fig. 4 presents the gas saturation profiles, with the water injection inlet on the left. At the low flow rate (Case 1, 0.01 mL/min), the residual gas saturation without pressure decline was approximately 0.37. When a pressure drop of 7.5% was imposed at this state with continued brine injection, the residual gas saturation increased slightly to ~ 0.40, an increase of $\sim 8\%$, similar to the pressure drop. Some dissolution is observed at the inlet side (dark blue) due to the large amount of brine injected. At the higher flow rate (Case 3, 0.05 mL/min), S_{gr} without pressure decline (light green) was similar to Case 1 (light blue). When the displacement is continued, this time with pressure decline (dark green), significant gas dissolution is observed due to the higher flow rate and larger volumes injected to reach the same fractional pressure drop as in Case 1. However, the outlet section of the sample showed a steady saturation as the brine had time to re-equilibrate during its passage through the rock. As the brine progresses through the sample, it re-equilibrates with H_2, so dissolution is strongest near the inlet and becomes negligible towards the outlet. Similar downstream re-equilibration behaviour has been reported in pore-scale imaging studies (Jangda et al., 2023). S_{gr} in Cases 1 and 3 (taken from the uniform saturation profiles) are almost identical; no further gas was displaced at the higher flow rate. Overall, the more uniform part of the sample showed similar gas expansion behaviour at both flow rates that is proportional to the pressure drop. This indicates that no significant gas was produced by expansion and that the invasion was mostly confined within the sample. In other words, if the expanded gas volume measured from the micro-CT images was proportionally smaller than the fractional pressure drop ($\Delta P/P$), the remaining expanded gas would have to have been produced through the outlet.

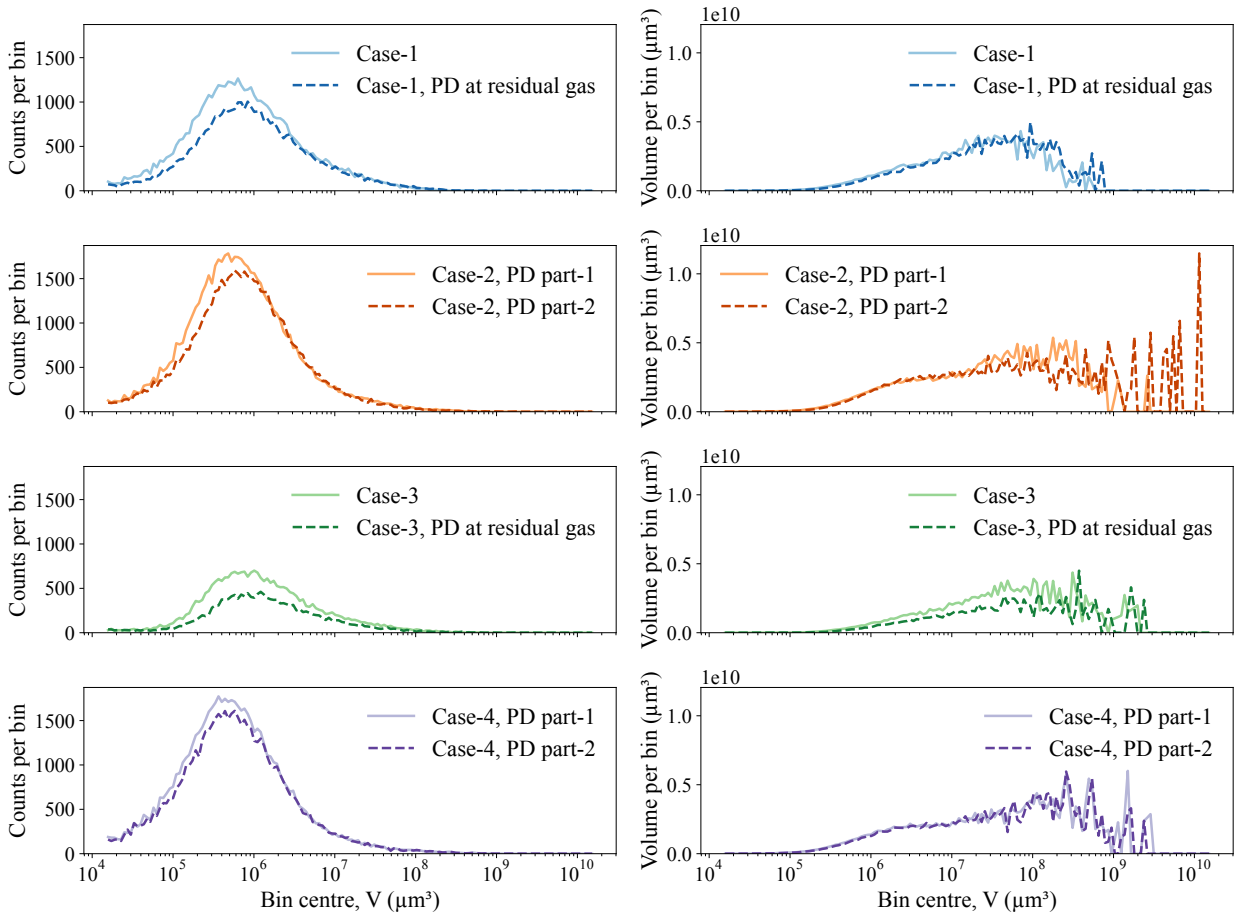

Fig. 5. Ganglia volume distributions expressed as the number of ganglia (left) and the gas volume (right) per logarithmic volume group ($\Delta \lg 0.04$).

The similar behaviour is observed in Cases 2 and 4, where pressure decline began at the start of brine injection (initial condition: S_{gi}), but with two notable differences. The first is the higher residual, or remaining, gas saturation observed. The remaining gas saturation after the initial pressure decline was 0.48 for the lower flow rate and 0.49 at the higher flow rate. At the lower flow rate, Case 2 (PD part-2), the pressure was reduced by approximately a further 23%, and the expanded gas volume increased by approximately 14%. The gas saturation increased from 0.48 to 0.55, which is above the residual saturation obtained by the case with no pressure decline (0.37). This indicates that a large portion of the gas was produced by expansion where gas left through the outlet, with limited direct displacement.

The high gas saturation (S_g reached 0.55 in Case 2 PD part-2) during pressure decline with a constant brine influx indicates that the local capillary pressure always increased (making displacement a drainage process). The gas continued to invade from each ganglion until the clusters connected to the outlet and were produced. At the field-scale, the outlet could resemble gas above the GWC, where the initially disconnected gas clusters below the GWC expand to connect to the mobile gas above it. Here, the high gas saturation (0.55) was not necessarily the maximum gas saturation. At larger pressure drops the measured S_g increase becomes smaller than the fractional pressure drop, indicating that part of the expansion is attributed to gas production. It is also possible that the gas reached the S_{gc} and the brine re-trapped it. Nonetheless, the S_{gc} at these conditions is expected to be larger than 0.55.

To further examine the trapping configuration after each displacement, the distribution of hydrogen ganglia volumes was analysed. This comparison helps distinguish whether differences in residual gas saturation arise from changes in the number of ganglia, their size, or both. Fig. 5 shows the volume distribution of hydrogen ganglia during the four displacements, expressed both as ganglia count (left panels) and gas volume (right panels). Cases 1 and 3 differed only in flow rate, yet Case 3 displayed almost half as many ganglia. This reduction is likely linked to enhanced H_2 dissolution at the higher flow rate, which can shrink and/or completely dissolve smaller trapped ganglia. Yet the gas-volume distribution (right panel) for Case 3 is not reduced by the same factor, indicating that at similar S_{gr} the trapped gas is redistributed into fewer, larger ganglia. In addition, increasing the flow rate may reduce snap-off events by not allowing enough time for the wetting layers to swell (Krevor et al., 2015), promoting a less fragmented trapped-gas configuration. Nonetheless, when pressure decline was imposed at residual gas saturation in both cases, the distributions shifted towards larger volumes despite the difference in flow rate.

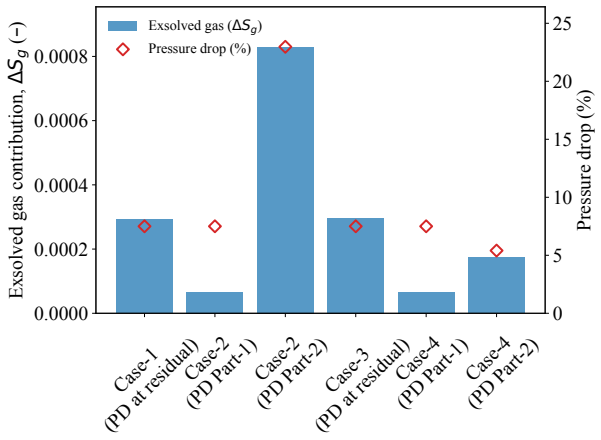

Fig. 6. Exsolved gas contribution to the measured gas saturation (ΔS_g, blue bars) following each pressure decline step. The right axis shows the corresponding fractional pressure drop (red markers). Labels on the *x*-axis indicate the displacement cases performed.

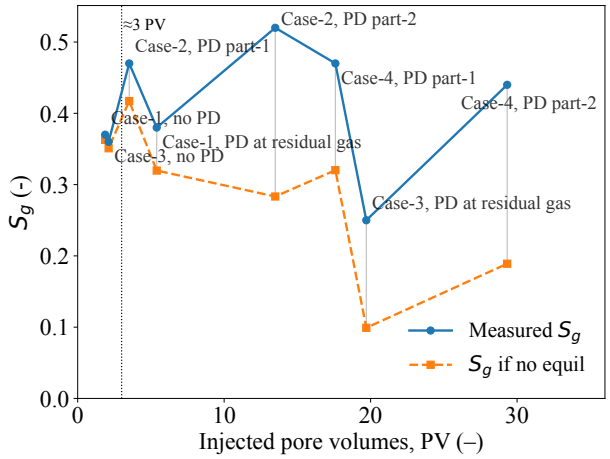

Fig. 7. Gas saturation during the displacements as a function of injected pore volumes. Blue markers show the measured values from the 3D images (average gas saturation), while orange markers indicate the expected gas saturation if the injected brine had not been pre-equilibrated with hydrogen.

In Case 2 (light orange), imposing pressure decline at the start resulted in a larger number of trapped ganglia than PD at S_{gr} (Case 1, light blue). In Case 4 (PD at S_{gi}), the higher flow rate produced a mixed response, with some groups growing while others shrinking. This points to multiple processes taking place simultaneously: Gas expansion and dissolution. From secondary drainage relative permeability tests in high permeability sandstones (Berea/Bentheimer) it is expected that the gas would be mobile at a saturation of 0.55 (Ruprecht et al., 2014). Therefore, if pressure decline was stopped, the system would no longer be under drainage displacement, and some gas is expected to be displaced by water during imbibition.

4.2 Gas exsolution

To assess whether dissolved hydrogen could significantly contribute to the expanded gas volume, the exsolved-gas fraction was estimated for each displacement. This allows the measured increase in gas saturation to be compared directly with the amount expected from gas exsolution. Fig. 6 shows the exsolved gas contribution to the gas saturation increase, ΔS_g, together with the pressure drop fraction for each displacement. The estimates use Henry's law and the brine mass taken from the baseline water saturation and pore volume (Eqs. (9) and (10)).

A key comparison is Case 1 (PD at S_{gr}) against Case 2, Part-1 (PD at S_{gi}). Both have a similar pressure drop fraction, yet ΔS_g is larger for Case 1. This is because the amount that can come out of solution is proportional to the volume of brine available. At a lower residual gas saturation, the water saturation is higher, and more dissolved H_2 can be released for the same $\Delta P/P_0$. As seen earlier, starting PD at the onset of brine injection resulted in a larger remaining gas saturation.

The overall exsolved gas contribution is small (order of 10^{-4}-10^{-3} in ΔS_g), even for the larger pressure drop. As expected in a H_2-brine system, exsolution is a secondary contribution compared with volume gas expansion. At the field-scale, it is not expected of exsolution to be of significance above the GWC due to the smaller volume of water. However, it may matter near the FWL, where the brine saturation is highest, especially if long production periods are expected and the pore pressure drop is large.

4.3 Gas dissolution during brine injection

To evaluate the effect of gas dissolution, the measured gas saturation was compared with the saturation predicted assuming no prior hydrogen equilibration. Fig. 7 shows this comparison between the average gas saturation measured from the images with the saturation expected if the brine had not been pre-equilibrated with hydrogen, estimated using Henry's law and the total injected pore volumes of brine, Eq. (9). At low injected pore volumes, less than about three PVs, the two lines almost overlap, showing that non-pre-equilibrated brine effect is negligible. This observation is consistent with Gao et al. (2023), who reported that noticeable dissolution effects appeared only after 2 PVs of non-pre-equilibrated brine injection.

As more brine is injected, and particularly as the system pressure declines, the gap between the two trendlines widens, most strongly at larger pressure drops. This indicates that the pre-equilibration procedure is not the issue; rather, the continued brine injection allows the slight equilibration offset in pressure between the trapped gases and the injected brine to accumulate, leading to progressive dissolution. Trapped ganglia can be at a pressure higher than the pore pressure, and the imposed pressure gradient during injection adds to this equilibration imbalance.

While pressure decline might be expected to reduce dissolution by lowering the equilibrium solubility, the situation is more complex at the pore-scale. While the disconnected gas ganglia's pressures are more or less constant in these

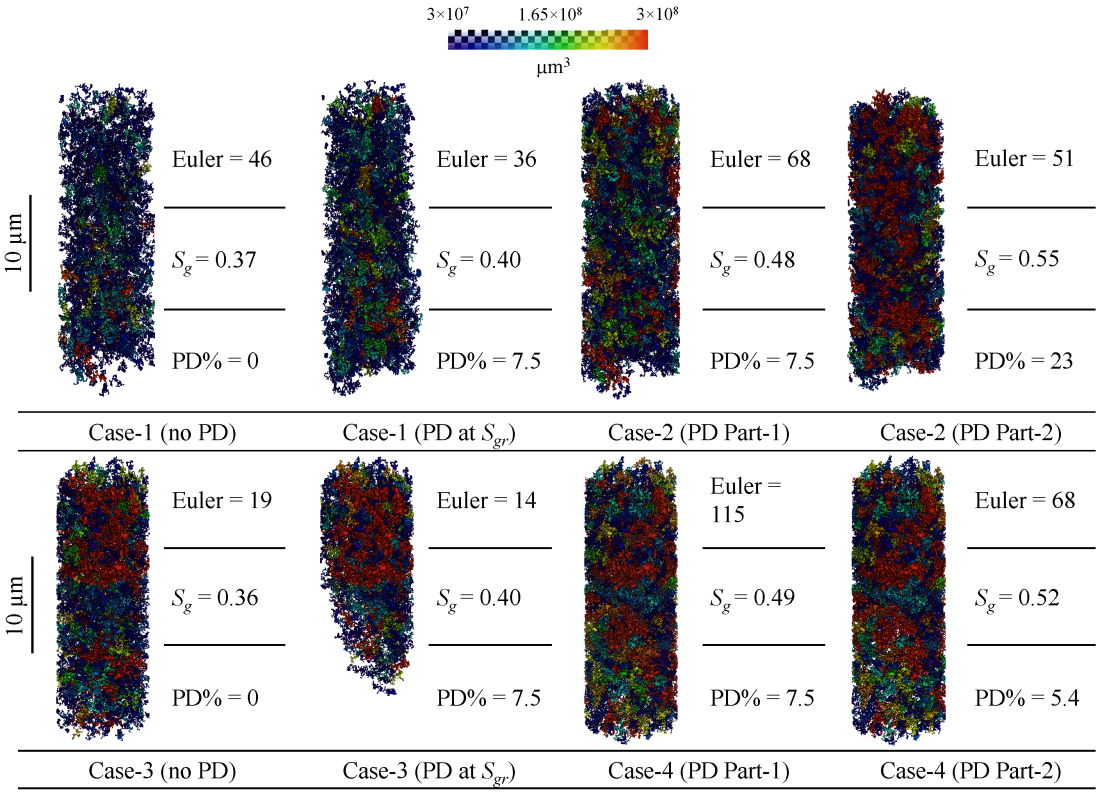

Fig. 8. Pore-scale images of hydrogen ganglia coloured by volume for all cases. The outlet/production is on the top side. Reported values include the rock normalised Euler characteristic (1/mm^3), the gas saturation S_g, and the applied fractional pressure drop, PD. The legend indicates the ganglion volumes in μm^3.

displacements, the brine pressure declines. This increases the pressure equilibration offset between the brine and gas phases, which can accelerate dissolution. On the other hand, if the gas is connected to the outlet, its pressure will decrease, and the equilibration pressure offset will decrease or remain constant (i.e., less gas dissolution).

The extent to which this phenomenon persists at the field-scale depends on phase connectivity and near-wellbore boundary conditions. In particular, after water breakthrough and loss of a continuous gas cap, the evolution of $P_g - P_w$ is dependent on whether gas remains connected to the wellbore or is fully trapped. Therefore, quantifying its impact on dissolution requires coupled flow-mass transfer modelling and/or field-scale data.

4.4 Gas connectivity and interfacial areas

To examine how pressure decline affected the spatial arrangement and connectivity of the trapped gas, the 3D distribution of the gas phase was visualised and quantified using the Euler characteristic. Fig. 8 shows all the 3D gas clusters larger than 3×10^7 μm^3, with smaller ganglia excluded for visual clarity to reduce visual clutter from the large population of very small clusters. This threshold does not affect the qualitative connectivity conclusions (i.e., connectivity metrics were assessed before the 3D visual rendering). The normalised Euler characteristic was measured in all displacements. The Euler characteristic provides a topological measure of connectivity. A positive Euler characteristic indicates that the gas phase is dominated by many disconnected ganglia (many discrete objects with few loops). In all cases, the Euler characteristic is positive, indicating poorly connected gas. Gas-phase connectivity improves after pressure decline. The shapes of the large gas clusters exceeding 3×10^8 μm^3 (red ganglia) after pressure decline highlight that expansion is not frontal, as in gas injection, but occurs volumetrically throughout the pore space. This resembles normal percolation, where each ganglion cluster invades neighbouring regions of the pore space independently. This was also shown in a previous study that compared gas drainage by injection with drainage by gas expansion, where more lateral invasion was observed during expansion and more frontal advance during injection (Dokhon et al., 2024). More importantly, starting PD at the beginning of brine injection produced larger residual gas ganglia, and a large gas cluster can be seen connected to the outlet (top side) for Case 3, PD part-2, where the largest pressure drop fraction (23%) was applied. PD at S_{gr} showed little gas connection, as evident from the small reduction in the Euler characteristic. This is because the gas remained trapped and simply expanded within the same pores or neighbouring pores without significant coalescence or invasion.

The effect of pressure decline on pore-scale fluid occupancy was assessed by comparing the gas-water (GW), gas-rock (GR), and water-rock (WR) interfacial areas for the different displacements. The results are shown in Fig. 9. As

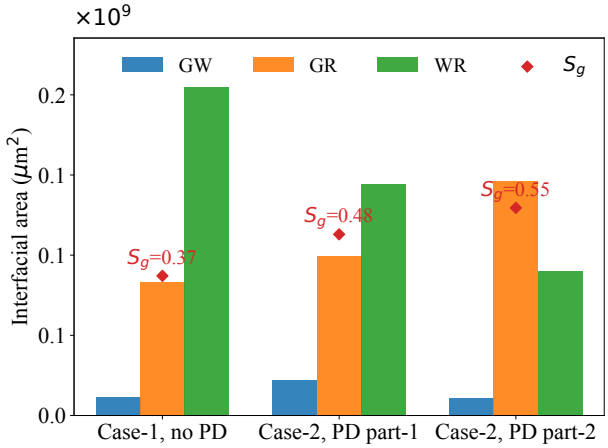

Fig. 9. Interfacial areas for gas-water (GW), gas-rock (GR), and water-rock (WR) contacts in cases 1 and 2. Red markers show the corresponding average gas saturations.

the gas saturation increases with pressure decline, GR generally increases while WR decreases, reflecting the greater pore occupancy of the expanding gas. The behaviour of GW is less straightforward: It can rise when many small, trapped ganglia remain, or drop when the GW interface moves into tighter pore spaces at higher S_g. Here, PD imposed at the start of brine injection produced a larger GW interfacial area compared to PD at residual. This can be explained by the larger number of ganglia observed in Case 2 PD Part-1 from Fig. 5. This may be linked to gas nucleation, creating more dispersed clusters. When PD continued (Case 2 Part-2), GW interfacial area decreased, indicating coalescence of clusters, the interface moving into smaller pore bodies, and greater capillary pressure driven by gas expansion.

5. Conclusions

A pore-scale experiment was designed to quantify and understand how pressure decline interacts with simultaneous brine injection during UHS withdrawal, and to re-evaluate the concepts of S_{gc} and gas remobilisation. Using micro-CT imaging of Bentheimer sandstone, displacements were measured at two flow rates (0.01 and 0.05 mL/min), a programmed pressure decline rate of 1 kPa/min was applied, and the impact of the timing of pressure decline (at S_{gi} vs S_{gr}) and the size of the pressure drop was studied. The displacement behaviour, gas connectivity, and interfacial areas were analysed. The effects of gas bulk expansion, exsolution, and dissolution were examined.

During pressure decline, the pore-scale displacement was drainage-dominated, even though brine was injected. Without pressure decline, brine injection led to a residual gas saturation of 0.37. When the pressure then declined, the gas expanded linearly with the pressure drop to reach a saturation of approximately 0.4: The gas remained disconnected. When pressure decline started from a high initial gas saturation, gas connected to the outlet was produced and the gas saturation reached 0.49 and 0.48 for the low and high flow rates, respectively. Further pressure decline led to an increase in gas saturation up to 0.55; the gas remained disconnected. During this second period of pressure decline, no displacement of gas by brine (imbibition) was observed, confirming that the system was always under drainage (with an increasing capillary pressure, P_c). This work suggests that the S_{gc} for flow can be very high (0.55 or larger) during pressure decline, even if brine is flowing. The results are consistent with measurements of a S_{gc} of approximately 0.61 for carbon dioxide, measured during pressure decline only with no injection (Moghadasi et al., 2025).

Ganglia statistics and connectivity analysis confirmed that pressure decline at the start of displacement created more and larger clusters of trapped gas. Exsolution of dissolved gas had a small impact (ΔS_g in the order of 10^{-4}-10^{-3}) and was more significant at lower gas saturations due to the available brine volume. Therefore, gas exsolution may be more noticeable near the FWL. Gas dissolution was observed at the inlet side and is directly linked to the amount of brine injected and pressure drop, caused by the pressure equilibration offset between the trapped gas bubbles and the reduction of the brine pressure. 3D images of the expanded gas showed that expansion invasion resembles normal percolation, with each ganglion percolating independently and expanding volumetrically.

For field applications and modelling, these results show that gas production during withdrawal is mainly driven by gas expansion, even in the presence of a brine pressure gradient. Trapped gases below the GWC expand locally as the brine pressure declines and connect to the continuous gas phase above it. The connected gas above the GWC then expands further towards the production well. This agrees with the mechanism reported by Alobaidan et al. (2025), who showed that, based on modelling studies, the gas expansion drive mechanism is the main contributor to hydrogen withdrawal in water-wet sandstone systems. S_{gc} when the gas is first connected across the systems depends on the displacement process, initial condition and pressure decline rate.

The results reported here were obtained in a relatively homogeneous, strongly water-wet sandstone rock. In more heterogeneous rocks (e.g., many carbonates), a broader pore-throat size distribution and spatial variability in capillary entry pressure can promote preferential invasion pathways and a broader trapped-cluster size spectrum, which may modify the apparent S_{gc} and the extent to which pressure decline expansion drives coalescence and reconnection. In mixed-wet systems, capillary trapping is commonly reduced, and the non-wetting phase may access smaller pores and maintain connectivity through layers, which could lower S_{gc} and increase the likelihood that expansion/coalescence creates connectivity.

Future work should extend this framework to conduct a steady-state relative permeability measurement to capture the gas relative permeability once it becomes mobile during pressure decline. Pore-network modelling can extend this work to broader conditions, such as varying temperatures, mixed wettability and heterogeneous rocks.

Acknowledgements

WD thanks Saudi Aramco for funding his PhD studies.

Supplementary file

The raw 3D TIFF image data supporting this study are openly available on https://doi.org/10.5281/zenodo.19463137

Conflicts of interest

The authors declare no competing interest.

References

Ahmed, T. Reservoir Engineering Handbook. Cambridge, MA, USA, Gulf Professional Publishing, 2018.

Al-Masri, W., Shapiro, A. Experimental determination of relative permeabilities and critical gas saturations under solution-gas drive. Journal of Petroleum Science and Engineering, 2021, 202: 108509.

Alobaidan, I. A., Bijeljic, B., Blunt, M. J. Drive mechanisms and hydrogen recovery in underground storage: A material balance and simulation approach. International Journal of Hydrogen Energy, 2025, 146: 149891.

Al-Yaseri, A., Esteban, L., Yekeen, N., et al. The effect of clay on initial and residual saturation of hydrogen in clay-rich sandstone formation: Implications for underground hydrogen storage. International Journal of Hydrogen Energy, 2023, 48(13): 5175-5185.

Andrew, M., Bijeljic, B., Blunt, M. J. Pore-scale contact angle measurements at reservoir conditions using X-ray microtomography. Advances in Water Resources, 2014, 68: 24-31.

Bagchi, C., Patwardhan, S. D., Iglauer, S., et al. A critical review on parameters affecting the feasibility of underground hydrogen storage. ACS Omega, 2025, 10(12): 11658-11696.

Baldwin, C. A., Sederman, A. J., Mantle, M. D., et al. Determination and characterization of the structure of a pore space from 3D volume images. Journal of Colloid and Interface Science, 1996, 181(1): 79-92.

Berg, S., Gao, Y., Georgiadis, A., et al. Determination of critical gas saturation by micro-CT. Petrophysics, 2020, 61(2): 133-150.

Brown, K., Schlüter, S., Sheppard, A., et al. On the challenges of measuring interfacial characteristics of three-phase fluid flow with X-ray microtomography. Journal of Microscopy, 2014, 253(3): 171-182.

Chabab, S., Théveneau, P., Coquelet, C., et al. Measurements and predictive models of high-pressure H_2 solubility in brine (H_2O + NaCl) for underground hydrogen storage application. International Journal of Hydrogen Energy, 2020, 45(56): 32206-32220.

Dokhon, W., AlZaabi, A., Bijeljic, B., et al. Micro-CT imaging of drainage and spontaneous imbibition for underground hydrogen storage in saline aquifers. Advances in Water Resources, 2025, 204: 105064.

Dokhon, W., Goodarzi, S., Alzahrani, H. M., et al. Pressure decline and gas expansion in underground hydrogen storage: A pore-scale percolation study. International Journal of Hydrogen Energy, 2024, 86: 261-274.

Drummond, A., Fishlock, T., Naylor, P., et al. An evaluation of post-waterflood depressurisation of the South Brae Field, North Sea. Paper SPE 71487 Presented at SPE Annual Technical Conference and Exhibition, New Orleans, Louisiana, 30 September-3 October, 2001.

Egermann, P., Vizika, O. Critical gas saturation and relative permeability during depressurization in the far field and the near-wellbore region. Paper SPE 63149 Presented at SPE Annual Technical Conference and Exhibition, Dallas, Texas, 1-4 October, 2000.

Gao, Y., Sorop, T., Brussee, N., et al. Advanced digital-SCAL measurements of gas trapped in sandstone. Petrophysics, 2023, 64(3): 368-383.

Heinemann, N., Alcalde, J., Miocic, J. M., et al. Enabling large-scale hydrogen storage in porous media-the scientific challenges. Energy and Environmental Science, 2021, 14(2): 853-864.

Higgs, S., Wang, Y., Sun, C., et al. Direct measurement of hydrogen relative permeability hysteresis for underground hydrogen storage. International Journal of Hydrogen Energy, 2024, 50: 524-541.

Jangda, Z., Menke, H., Busch, A., et al. Pore-scale visualization of hydrogen storage in a sandstone at subsurface pressure and temperature conditions: Trapping, dissolution and wettability. Journal of Colloid and Interface Science, 2023, 629: 316-325.

Kamath, J., Boyer, R. Critical gas saturation and supersaturation in low-permeability rocks. SPE Formation Evaluation, 1995, 10(4): 247-253.

Krevor, S., Blunt, M. J., Benson, S. M., et al. Capillary trapping for geologic carbon dioxide storage - from pore scale physics to field scale implications. International Journal of Greenhouse Gas Control, 2015, 40: 221-237.

Miocic, J., Heinemann, N., Edlmann, K., et al. Underground hydrogen storage: A review. Geological Society, London, Special Publications, 2023, 528(1): 73-86.

Moghadasi, R., Foroughi, S., Goodarzi, S., et al. Trapping and remobilization during geological CO_2 storage: A pore-scale imaging and modeling study. Advances in Water Resources, 2025, 205: 105092.

Mwakipunda, G. C., Kouassi, A. K. F., Ayimadu, E. T., et al. Underground hydrogen storage in geological formations: A review. Journal of Rock Mechanics and Geotechnical Engineering, 2025, 17(10): 6704-6741.

Naylor, P., Fishlock, T., Mogford, D., et al. Relative permeability measurements for post-waterflood depressurisation of the Miller Field, North Sea. Paper SPE 63148 Presented at SPE Annual Technical Conference and Exhibition, Dallas, Texas, 1-4 October, 2000.

Peksa, A. E., Wolf, K. H. A. A., Slob, E. C., et al. Original and pyrometamorphical altered Bentheimer sandstone; petrophysical properties, surface and dielectric behavior. Journal of Petroleum Science and Engineering, 2017, 149: 270-280.

Peksa, A. E., Wolf, K. H. A. A., Zitha, P. L. J. Bentheimer sandstone revisited for experimental purposes. Marine

and Petroleum Geology, 2015, 67: 701-719.

Petersen Jr, E. B., Agaev, G. S., Palatnik, B., et al. Determination of critical gas saturation and relative permeabilities relevant to the depressurization of the Statfjord Field. Paper SCA2004-33 Presented at International Symposium of the Society of Core Analysts, Abu Dhabi, UAE, 5-9 October, 2004.

Raeesi, B., Morrow, N. R., Mason, G. Capillary pressure hysteresis behavior of three sandstones measured with a multistep outflow–inflow apparatus. Vadose Zone Journal, 2014, 13(3): 1-12.

Ruprecht, C., Pini, R., Falta, R., et al. Hysteretic trapping and relative permeability of CO_2 in sandstone at reservoir conditions. International Journal of Greenhouse Gas Control, 2014, 27: 15-27.

Sun, X., Zhang, Y., Wang, S., et al. Experimental study and new three-dimensional kinetic modeling of foamy solution-gas drive processes. Scientific Reports, 2018, 8(1): 4369.

Zhu, Z., Cao, Y., Zheng, Z., et al. An accurate model for estimating H_2 solubility in pure water and aqueous NaCl solutions. Energies, 2022, 15(14): 5021.

Zivar, D., Kumar, S., Foroozesh, J. Underground hydrogen storage: A comprehensive review. International Journal of Hydrogen Energy, 2021, 46(45): 23436-23462.

Zuo, L., Krevor, S., Falta, R. W., et al. An experimental study of CO_2 exsolution and relative permeability measurements during CO_2 saturated water depressurization. Transport in Porous Media, 2012, 91(2): 459-478.